Volume 14
Number 32
28 August 2022
Pages 11473-11792

Nanoscale

rsc.li/nanoscale

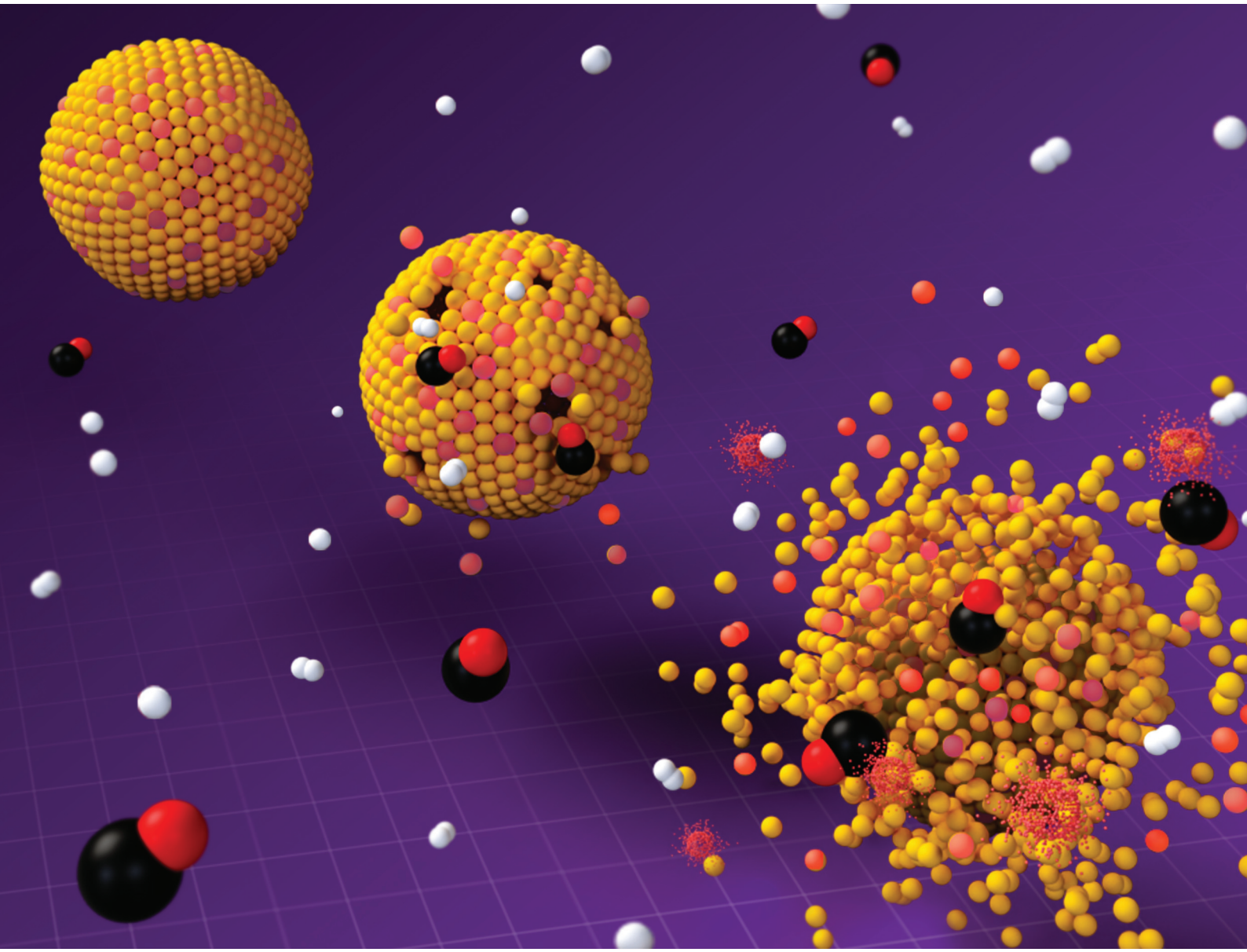

ISSN 2040-3372

ROYAL SOCIETY OF CHEMISTRY

PAPER

Alba Garzón Manjón, Christina Scheu *et al.*
Evaluation of functional layers thinning of high temperature polymer electrolyte membrane fuel cells after long term operation

NCNST

Nanoscale

PAPER

View Article Online
View Journal | View Issue

Cite this: *Nanoscale*, 2022, **14**, 11543

Evaluation of functional layers thinning of high temperature polymer electrolyte membrane fuel cells after long term operation†

Miquel Vega Paredes, ‡[a] Alba Garzón Manjón, *‡[a] Bjoern Hill,§[a] Torsten Schwarz,[a] Nicolas A. Rivas,[a] Tilman Jurzinsky,[b] Katharina Hengge,[b] Florian Mack[b] and Christina Scheu *[a]

The operation related degradation processes of high temperature polymer electrolyte membrane fuel cell operated with hydrogen-rich reformate gas are studied. CO impurities from the reformate gas are strongly adsorbed by the catalyst surface, leading to poisoning and thus, reduction of the overall performance of the cell. Most of the studies are performed in a laboratory set-up by applying accelerated stress tests. In the present work, a high temperature polymer electrolyte membrane fuel cell is operated in a realistic configuration for 12 000 h (500 days). The fuel cell contains as electrocatalyst Pt in the cathode and a Pt–Ru alloy in the anode. The study of the degradation occurring in the functional layers, *i.e.* in different regions of cathode, anode and membrane layer, is carried out by scanning electron microscopy, (scanning) transmission electron microscopy and energy dispersive X-ray spectroscopy. We observed a thinning of the functional layers and a redistribution of catalyst material. The thinning of the cathode side is larger compared to the anode side due to harsher operation conditions likely causing a degradation of the support material *via* C corrosion and/or due to a degradation of the catalyst *via* oxidation of Pt and Ru. A thinning of the membrane caused by oxidation agents is also detected. Moreover, during operation, catalyst material is dissolved at the cathode side and redistributed. Our results will help to design and develop fuel cells with higher performance.

Received 25th May 2022,
Accepted 5th July 2022

DOI: 10.1039/d2nr02892a

rsc.li/nanoscale

1. Introduction

Climate change is nowadays one of the biggest challenges of our society. The effects of elevated concentrations of CO_2 in the atmosphere include the raise of global temperature, altered precipitation and increased frequency of extreme climatic events. Therefore, there is a strong need to reduce CO_2 and other greenhouse gas emissions. Electricity/heat production and transport are the two sectors that emit most CO_2,[1] and as such it is key to reduce greenhouse gas emissions in those sectors. A promising technology to replace combustion engines in electricity generation and transport applications is based on fuel cells (FCs).[2,3] FCs are electrochemical devices which continuously convert the chemical energy of an externally supplied fuel and oxidant to electrical energy.[4] If H_2 is used as a fuel, the main product generated is water, and no greenhouse gases are emitted during FC operation. Thus, FCs are highly efficient and clean energy converting devices. Other advantages of FCs include their high power density, safe operation, low noise generation, and low maintenance requirements.[5]

In this work, the focus lies on high temperature proton exchange membrane FCs, so-called high temperature polymer electrolyte membrane FCs (HT-PEMFCs). These devices are particularly attractive for home-based power generation, transportation and other portable applications.[6] Some of their appealing features include high efficiency, rapid start-up, and a higher tolerance to impurities in the reactants.[6] This last point is especially remarkable, since the HT-PEMFCs studied in this work used reformate gas as a fuel. Reformate is a hydrogen-rich gas originating from the steam reforming of carbohydrates, and contains traces of CO. CO is an impurity that is known to adsorb strongly onto the surface of Pt, poisoning it and impacting the overall performance of the cell.[7] Pt is the

[a]*Max-Planck-Institut für Eisenforschung GmbH, Max-Planck-Straße 1, 40237 Düsseldorf, Germany. E-mail: a.garzon@mpie.de*
[b]*Freudenberg Fuel Cell e-Power Systems GmbH, Bayerwaldstraße 3, 81737 München, Germany*

†Electronic supplementary information (ESI) available. See DOI: **https://doi.org/10.1039/d2nr02892a**

‡Equal contribution.

§Present address: Physical Chemistry II Department, Faculty of Chemistry and Biochemistry, Ruhr Universität Bochum, Universitätsstraße 150, 44801 Bochum, Germany.

most commonly used electrocatalyst in PEMFCs due to its high efficiency.[8] A catalyst is needed in both the cathode and anode to enhance the oxygen reduction reaction (ORR) and the hydrogen oxidation reaction (HOR), respectively. Since the CO present in the fuel can poison Pt in the anode, anode catalysts can combine Pt with other transition metals to mitigate this effect. It has been reported that alloying Pt with Ru enhances notably the CO tolerance by two different effects, namely the electronic and the bifunctional effect.[9] In the electronic effect, Ru modifies the band structure of Pt, reducing its affinity towards CO, while in the bifunctional Ru helps in the catalysis of CO oxidation to CO_2, which has a lower affinity for the catalyst.

One of the biggest challenges for the widespread commercialization of PEMFCs is their limited durability, since their efficiency decreases during operating time as a consequence of different degradation processes. There are many studies that try to understand the mechanisms behind such degradation processes. A lot of these studies focus on the catalyst degradation,[10–13] since catalyst particles agglomeration or dissolution are well known phenomena that decrease the active surface area of the electrode and impact the cell performance. Other studies focus on the carbon corrosion, especially on the cathode, where the higher potential makes the oxidation of the C support to CO_2.[14]

However, most of these studies are done in laboratory setups, where only the catalyst particles themselves and the support material are analysed.[15–18] In other studies, the whole membrane electrode assembly (MEA) is studied after applying some sort of accelerated stress test (ASTs).[19–22] Thus, not many studies analyse PEMFC degradation after operation in realistic conditions for thousands of hours.[23] Furthermore, in these long-term studies, the inhomogeneities in the degradation process (*e.g.* how it varies among different positions in the cell) are typically not considered. It is well known that different positions in a PEMFC present different degrees of degradation which depend on their relative position to the O_2 and H_2 supply (cathode and anode inlet, respectively).[20,24] Obermaier *et al.*[25] addressed the degradation under realistic automotive conditions of a low temperature PEMFC stack, studying the inhomogeneities between different cells in the stack and within a given cell. However, under automotive conditions fuel starvation events associated with the start-up and shutdown of the cell are more common than under a constant load. Furthermore, in the system investigated by Obermaier *et al.*[25] Pt catalyst is used as electrocatalyst for both electrodes.

In the present work, the operational related degradation suffered by a HT-PEMFC operated in a realistic FC configuration for 12 000 h (500 days) is analysed. The studied cells contained Pt as electrocatalyst in the cathode and a PtRu alloy in the anode. Special focus lied on studying locally the changes in the functional layers during operation, to assess the inhomogeneities in the degradation suffered. Scanning electron microscopy (SEM) and energy dispersive X-ray spectroscopy (EDX) are used to determine the morphological and compositional changes of the functional layers (FLs) (cathode and anode catalyst and membrane layer). Furthermore, the compositional and structural changes of the catalyst nanoparticles (NPs) are investigated at higher magnification by coupling (scanning) transmission electron microscopy ((S)TEM) with EDX and electron diffraction (ED). Understanding the degradation at various length scales is key to the development of FC with better performance and increased lifetime.

2. Results

2.1. Fuel cell system

A single HT-PEMFC has a voltage below 1 V in a real operation, hence, for its application several single cells are combined to a macroscale fuel cell stack. A schematic top-view on a single HT-PEMFC from such a stack is shown in the ESI, Fig. SI1.† The functional parts of the fuel cell are enclosed by a frame. A bipolar plate is placed on top of the cell to provide oxygen at the cathode and one bipolar plate on bottom of the cell to provide hydrogen at the anode. Furthermore, gas in-/out-let pipes run through the cut-outs on the frame of fuel cells and bipolar plates.

The HT-PEMFC have been subjected to long term operation. The durability is shown in Fig. 1, where the voltage change at constant current is plotted. The small slop of the curve indicates that the HT-PEMFC has some performance loss over the time span of 12 000 h, but it is not severe, and the fuel cells can be still operated. The observed changes in performance with time are due to microstructural changes as discussed below.

2.2. SEM characterization

2.2.1. HT_non_operated. The first sample investigated is the HT_non_operated, which shows the microstructure and condition of the HT-PEMFC before operation. The backscattered electron (BSE) image displayed in Fig. 2 shows a cross section taken close to the cathode inlet. The other two studied regions of the same cell (centre of the cell and close to the anode inlet) did not show any significant difference from the region depicted in Fig. 2, as is expected by the fact that this cell had not been operated.

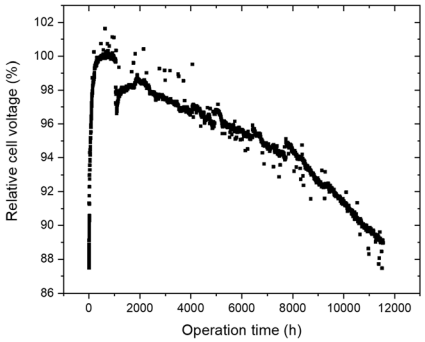

Fig. 1 Voltage response at constant current during HT-PEMFC operation.

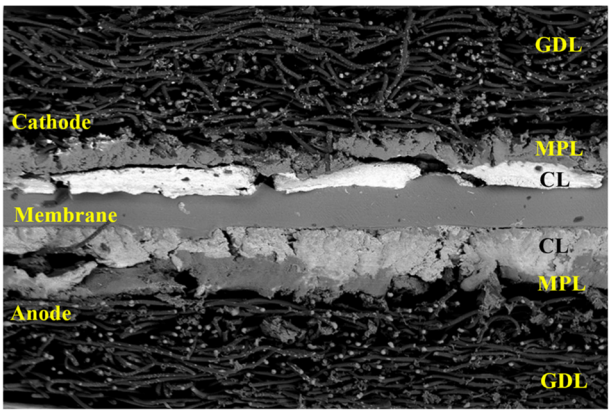

Fig. 2 SEM cross section image using BSE of the HT_non_operated cell. GDL: gas diffusion layer, MPL: microporous layer and CL: catalyst layer.

Regarding the structure of the FC, the gas diffusion layers (GDL) can be readily distinguished since it is made up of carbon fibres and constitutes the outer-most layer of the electrode. BSE images were recorded to distinguish cathode and anode. In this regard, the cathode appears brighter than the anode in BSE images which is attributed to the different composition and loading of the anode. Pt has a higher atomic number than the Pt–Ru alloy and thus appears brighter in the BSE images (Z contrast). The thickness of all three layers, *i.e.* cathode, membrane, and anode fluctuate in a range of ±10% along the cross-sectional surface due to the fabrication process.

The membrane has the largest layer thickness (51%) of the total FLs thickness. The anode and the cathode catalyst layer accounts for 31% and 18%, respectively of the total thickness. All differences in the average layer thickness are within the measurement uncertainty and hence, a spatially constant layer thickness is estimated.

2.2.2. HT_operated. The second sample investigated by SEM is the HT-PEMFC operated for 12 000 h. The structure of HT_operated cell can be compared to the reference of the HT_non_operated cell as it contains all functional layers even after operation of 12 000 hours. The BSE images obtained from the HT_operated cell showed that there were significant differences between the three different regions as is apparent from Fig. 3.

The BSE images of Fig. 3 shows that all the FLs have become thinner due to the FC operation. Additionally, several differences were observed between all the layers and the different regions. In some regions, gaps were found between the membrane and the cathode side, which suggests that the membrane degrades on the cathode side. Two different reasons are responsible for the gap between membrane and cathode: (i) during the operation the membrane partially lost phosphoric acid and shrank. The loss of phosphoric acid is more pronounced on the cathode side due to product water generation. (ii) The thinning of the cathode catalyst layer due to carbon corrosion.

After operation of the FC for 12 000 h the cathode suffered a pronounced degradation and is not as well defined as it was in the HT_non_operated (compare Fig. 2 and 3). In some regions the width of the cathode does not change during operation, whereas in other positions the cathode was practically completely removed. This phenomenon is especially relevant in the specimen taken from the cathode inlet region (Fig. 3c). Moreover, the thickness of the anode layer appears to have less degradation even if it is slightly thinner than before operation.

In order to achieve quantitative results on the degradation of the HT_operated cell, the thinning of the membrane was measured together with the change in width of the anode and the cathode (Fig. 4).

For the non-operated HT-PEMFC, the thickness of the FLs is constant along the fuel cell. During regular operation, the cathode thickness decreases to values between 15–65% of the initial thickness. The degree of thinning is stronger on the region closer to the cathode inlet of the HT-PEMFC. Moreover, the anode thickness decreases to values between ~65% and ~85% of the initial thickness. Moreover, on the anode, the thinning is more pronounced on the region closer to the cathode inlet of the HT-PEMFC as well.

The measurements pertaining to the cathode have the highest standard deviation: 76% in the anode inlet side, 84% in the center and 81% in the cathode inlet side. Furthermore, the cathode closer to the cathode gas inlet region is not as well defined as the rest of the components. In some sections, a

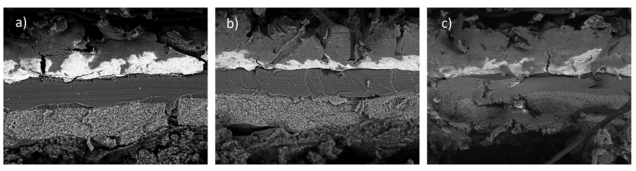

Fig. 3 BSE images from the HT_operated fuel cell after 12 000 h. The images correspond to samples taken from: (a) closer to the anode inlet, (b) center region and (c) closer to the cathode inlet.

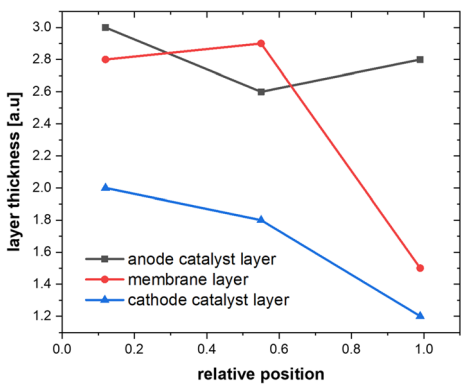

Fig. 4 Average thickness of the functional layers cathode, membrane and anode of the HT_operated cell. The thickness is given in a.u. The relative position is related to anode inlet (left) and cathode inlet (right). The lines are only to guide the eye and are no related to experimental data points.

thin layer can still be detected, while in others it is completely removed. Thus, the standard deviation from the measurements of the cathode (CL) increases considerably in this case. Fig. 3 shows the average thickness of the FLs along the FC.

The EDX spectrum (ESI Fig. SI2†) from the HT_non_operated cell shows the presence of C, O, F, P, Pt and Ru. The C signal originates from the membrane, which is composed of the organic polymer polybenzimidazole (PBI), a high surface area carbon (HSAC) support of the catalyst layer, and from the carbon fibres constituent of the GDL. The MPL consist of a low surface carbon and polytetrafluoroethylene, which explains the presence of C and F in that layer. Moreover, the CL is made up of a fluoropolymer which acts as a hydrophobic binder material. This explains the presence of F as well in the map. The P signal is due to the phosphoric acid doping of the PBI membrane. The acid doping is done in order to enhance proton conductivity. Finally, Pt and Ru are present in the cell as they are used as catalysts material.

EDX maps of Pt and Ru were recorded to better understand the catalyst distribution and degradation process after 12 000 h operation. The EDX elemental maps of the non-operated cell (Fig. 5a and b) show that Pt can be found in both CL with a higher loading in the cathode side as was expected Furthermore, the EDX analysis allows to distinguish the distribution of Ru and Pt, confirming that Ru is found exclusively in the CL of the anode of the non-operated cell. The EDX analysis allows only a qualitative analysis of Pt instead of quantitative due to the overlapping lines of P Kα (2.013 keV) (membrane component) and Pt M (2.048 keV). Nevertheless, it can be used to distinguish between anode and cathode. The anode catalyst layer contains the alloy made up of PtRu. The counts for Pt and Ru detected in the membrane and MPL were attributed to noise.

The EDX maps of the HT_operated cell is depicted in Fig. 5c and d. The EDX mapping of Pt shows the thinning of the catalyst layers after 12 000 h operation time. Especially, for the cathode catalyst layer which contains the highest amount of Pt, it can be observed that the layer thickness is significantly thinner compared to the non-operated HT-PEMFC (Fig. 5a). However, Pt can only be detected within both catalyst layers. Even after 12 000 h of operation, there is no area with a high Pt concentration outside the catalyst layers. From the Ru EDX mapping, no high level of thinning can be detected at the anode catalyst layer.

The anode catalyst layer contains both catalyst materials, Pt and Ru. Compared to the non-operated HT-PEMFC, the ratio Pt/Ru differs. Specifically, after 12 000 h of operation, the content of Pt is 7 times higher than the content of Ru. Moreover, a PtRu band can be detected in the membrane close to the cathode side, formed by the dissolution and reprecipitation of catalyst material during operation.

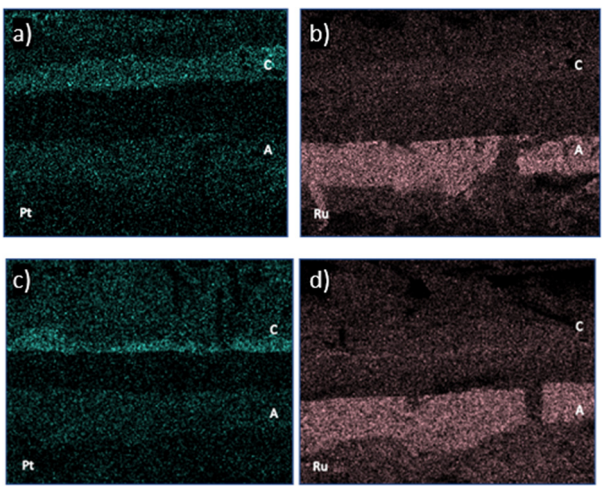

Fig. 5 EDX maps acquired across the different functional layers showing Pt (in green) and Ru (pink) distribution in HT_non_operated (a and b) and HT_operated (c and d). Close to the cathode layer, a band containing Ru and Pt is visible.

2.3. STEM characterization

STEM-HAADF images and EDX elemental distribution maps from the anode and cathode region of the HT_non_operated (Fig. 6a–d) show RuPt alloy NPs and pure Pt NPs with an average size of 5.1 ± 0.6 nm and 2.0 ± 0.5 nm, respectively. No Ru signal was detected on the cathode side of the HT_non_operated cell. The HT_operated cell shows significant differences in the size distribution and composition of the NPs in comparison with the HT_non_operated cell (see Fig. 6e–h). Firstly, the size distribution of PtRu alloy NPs on the anode is reduced leading to a bimodal system with two different average sizes: 4.4 ± 1.1 nm and 1.8 ± 0.5 nm (Fig. SI3†). Moreover, the average size of the Pt NPs on the cathode is increased to 8.1 ± 1.6 nm. Secondly, the PtRu alloy NPs lost 25% of the initial Ru. Furthermore, we found an increment of 3% of Ru at the cathode side. As visible in Fig. 6h, Ru single atoms (red) segregated on the surface of the pure Pt NPs of the cathode. Finally, Ru from the anode diffuses through the membrane and forms a PtRu alloy band. The average size of these NPs is 4.2 ± 0.8 nm with an Ru content up to 33%.

2.4. TEM characterization

TEM images and ED patterns from the anode and cathode region of the HT_non_operated (Fig. 7a–d) and HT_operated (Fig. 7e–h) cells were recorded to study the crystalline structure of the catalyst NPs. ED has the advantage over other diffraction techniques (such as X-ray diffraction) of being able to analyse the crystalline structure locally. Furthermore, with ED the crystalline structure of the NPs forming the PtRu band within the membrane after operation could be resolved.

The PtRu alloy NPs present in anode of HT_non_operated were found to have or hexagonal close packed (hcp) (Fig. 7a and b) ($d_{(010)}$ = 2.38 Å, $d_{(002)}$ = 2.141, $d_{(01-1)}$ = 2.082, $d_{(01-2)}$ = 1.592)[15] or face centered cubic (fcc) structure ($d_{(111)}$ = 2.265, $d_{(020)}$ = 1.962, $d_{(220)}$ = 1.387, $d_{(113)}$ = 1.183) depending on the Ru amount. On the other hand, the Pt NPs of the cathode of this cell were (fcc) (Fig. 7c and d).[15]

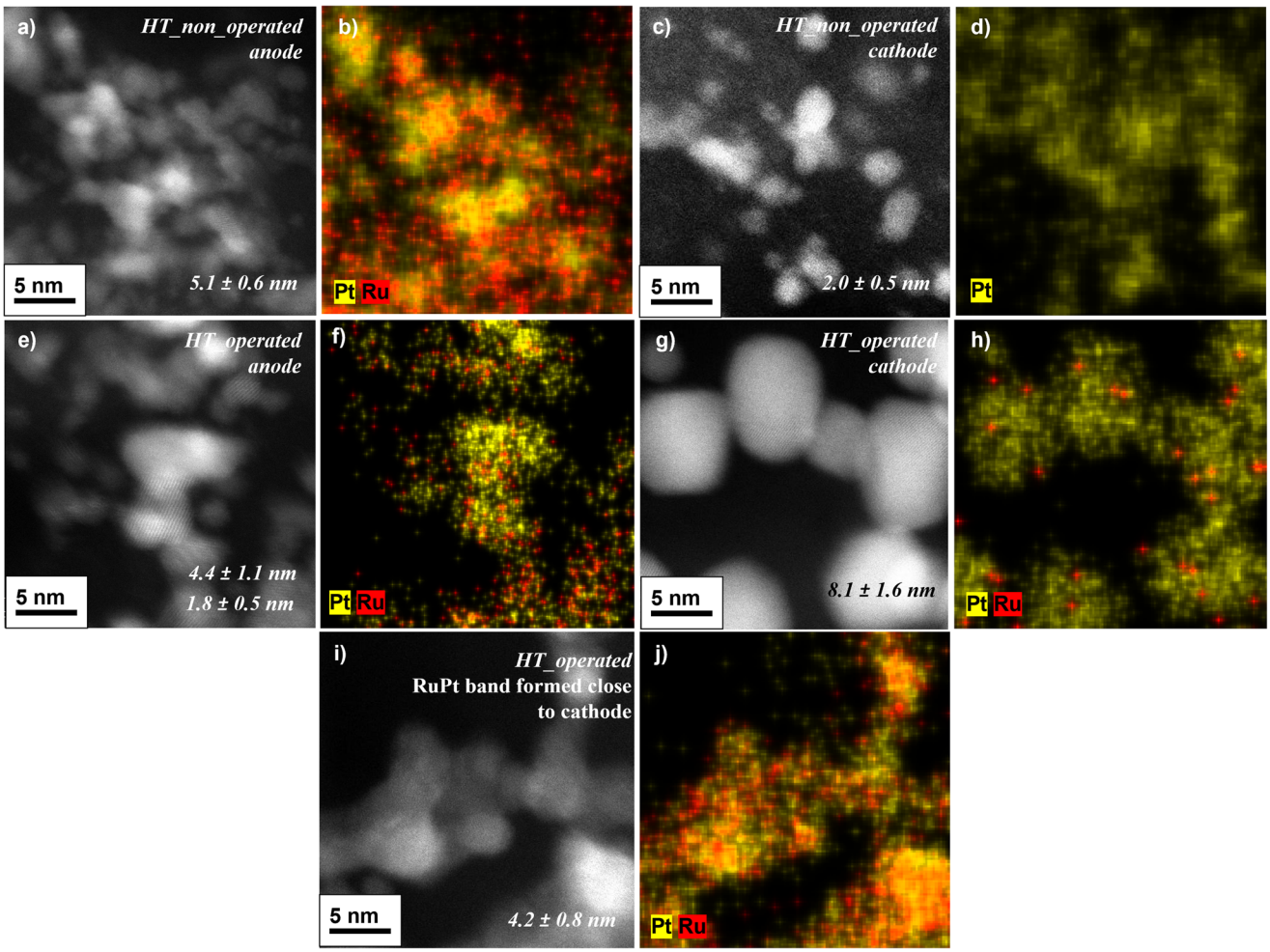

Fig. 6 STEM-HAADF-EDX characterization of the catalytic NPs before and after operation. HAADF images of HT_non_operated cell from anode (a) and cathode (c), and corresponding EDX measurements (b) and (d), respectively. HAADF images of HT_operated cell from anode (e) and cathode (g), as well as the corresponding EDX (f and h). In (i) and (j) HAADF images and EDX maps from the NPs forming the PtRu band within the membrane, close to the cathode after HT operation.

Besides the compositional changes observed in STEM-EDX (Fig. 6), significant structural changed also take place in the catalyst NPs during the 12 000 h of operation time, especially on the anode.

The PtRu alloy NPs present in this electrode are found to be only fcc in HT_operated (Fig. 7e and f). Moreover, in the cathode the catalyst NPs remain fcc after operation (Fig. 7g and h). Additionally, for PtRu band NPs both fcc and hcp reflections were detected in their ED patterns (Fig. 7i and j).

3. Discussion

The results show that two different degradation mechanism occur during operation of the HTPEMFC: (i) thinning of the FLs and (ii) catalyst material redistribution. These degradation process can be attributed to the 12 000 h operation time.

Thinning of the catalyst layers during HT-PEMFC operation has been reported in real operation as part of a fuel cell stack with HT-PEMFC similar to the cells investigated in this work. Hengge *et al.*[11] found comparable results for the phenomena of catalyst layer thinning with a stronger effect on the cathode side. However, the authors did not specify the operating time of the cell, and did not study if such degradation was position dependent within a given cell. There are different mechanisms that can lead to a stronger degradation process on the region closer to the cathode than the anode side:[26,27] (i) degradation of the carbon support material and (ii) degradation of the catalyst material itself:

Related to (i): at the anode and cathode catalyst layers, the Pt (cathode) or PtRu alloy (anode) catalyst material is present as nanoparticles on the surface of HSAC. At the cathode, the HSAC is exposed to strong oxidizing conditions (*e.g.* H_2O_2, HO_2^-, among other subproducts generated during ORR) which can lead to carbon corrosion.[28,29] With water as an oxidation agent, C can be oxidized to produce CO_2.[30] Thus, the reaction is possible at the cathode during operation of the HT-PEMFC since the thermodynamic potential of this reaction can be

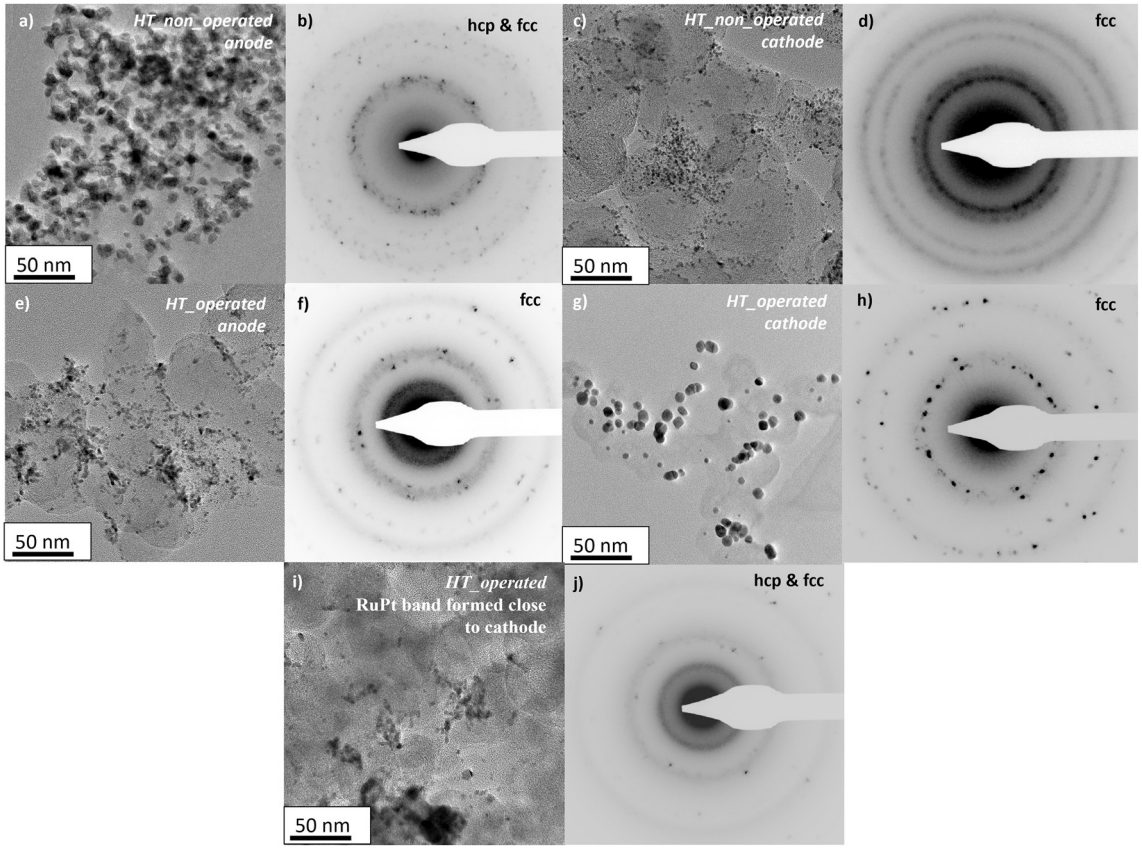

Fig. 7 TEM-ED characterization of the catalytic NPs before and after operation. TEM images of HT_non_operated cell from anode (a) and cathode (c), as well as the corresponding ED measurements (b) and (d), respectively. TEM images of HT_operated cell from anode (e) and cathode (g), as well as the corresponding ED measurements (f) and (h), respectively. TEM image (i) and corresponding ED measurements (j) from the NPs forming the PtRu band.

below the operation voltage. Even if the kinetics of this reaction are slow at the operation temperatures of the HT-PEMFC, during the start/stop cycling process potential excursions can occur leading to an increase of the reaction rate.[30] Furthermore, Pt can catalyze the C corrosion reaction as well generating a loss of the catalyst material attached to the support material.[31] The removed catalyst material can be redistributed to other areas of the HT-PEMFC or leave the FC (*e.g.* with the discharged water that is produced during fuel cell operation). Moreover, these oxidizing agent can play an important role in the thinning of the membrane that could lead to an increase leakage current through it.[32]

Regarding (ii) dissolution and redeposition of catalyst particles are well known mechanisms which occur during FC operation.[33] Under the working conditions, *e.g.* low pH value, high voltage potentials and temperatures, *etc*., the oxidation and dissolution of the catalyst material can take place. Due to the higher potential on the cathode side the dissolution and redeposition of catalyst material is stronger.[34] STEM-HAADF images in Fig. 6g show a severe Ostwald ripening effect of the Pt NPs after 12 000 h operation time. In addition, often the formation of a catalyst band within the membrane is observed which consists of PtRu alloy NPs.[11] The EDX maps also indicate the formation of such a band in the present sample (Fig. 5 and 6). Moreover, in the anode side, the degradation of the PtRu alloy NPs is also observed. The Ru amount is decreased as well as the average NPs size. We find a bimodal average size distribution which confirm the dissolution effect.

TEM-ED characterization demonstrates a phase transition on the hcp PtRu alloy NPs at the anode side to fcc after 12 000 h operation. This phenomenon can be related to the loss of Ru during operation. Moreover, the variation in crystalline structure (hcp and fcc) within the PtRu band NPs can be as well explained by their differences in composition. During operation Pt species from the cathode and PtRu species from the anode get dissolved and reprecipitate within the membrane.[11] Depending on the composition of individual particles (*i.e.*, they have a higher or lower Ru content), the hcp or fcc crystalline structure will be the most thermodynamically stable one and forms within the membrane.[15]

During FC operation, the temperature, O and H supply or the externally applied pressure should be constant for all areas. However, in real FC operation inhomogeneities occur which lead to fluctuations in the degree of degradation along the FC stack.[35,36] Local inhomogeneities in HT-PEMFC operations were investigated in previous studies.[37] The level of

degradation is found to differ depending on the operation conditions (*e.g.* it can be stronger close to the cathode inlet and anode outlet). Durst *et al.*[28] reported that during an aging test of PEMFC operation in start-up and shutdown conditions, a higher performance loss was found combined with a stronger thinning of the cathode catalyst layer close to the cathode inlet and anode outlet.

Inhomogeneities in performance losses and the level of CO poisoning were found during an aging test at constant load. Stronger losses were observed close to the cathode inlet and anode outlet, but cathode catalyst degradation was found to be stronger close to the cathode outlet.[38] These effects lead to possible degradation mechanisms, which can be influenced by the gas flow. Close to the cathode inlet, the O partial pressure is the highest, while it decreases towards the area close to the cathode outlet. Thus, the current density generated during fuel cell operation is higher close to the cathode inlet. This may increase the level of degradation closer to the cathode inlet.[38]

The HT-PEMFCs investigated in this work are operated using H_2 generated by steam reforming which contains CO impurities. The effect of CO poisoning is expected to occur in regions closer to the anode inlet. This effect may lead to a lower efficiency of the anode catalyst due to its degradation close to the anode inlet and hence, to a lower overall fuel cell performance.[38,39] Furthermore, it is known that a significant part of degradation is caused during start or stop cycles of the FC.[40] During start of the fuel cell operation, a reverse-current decay mechanism was proposed to describe an observed stronger degradation.[41] Degradation can be caused by the anode catalyst layer being partially filled with H_2 and O_2.[42] The O_2 crossover from the cathode side is enough to fill the anode catalyst layer with O_2 before startup. Moreover, when H_2 is led to the anode catalyst layer from the anode inlet, it can divide the fuel cell in two different parts (one active part close to the anode inlet and one passive part close to the anode outlet). At the passive part, reverse currents are generated, that leads to a significant drop of the anode potential while at the active part, the fuel cell is operating regularly. The increased potential difference between anode and cathode difference can lead to rapid O evolution and C corrosion, damaging the cathode electrode structure.

4. Experimental details

4.1. Investigated samples

The fuel cells were operated under constant load at a current density of 0.2 A cm^{-2} at 160 °C. Reformed natural gas on the anode with a stoichiometry of 1.4 and air at the cathode with a stoichiometry of 2.0 were used for the long-term operation. HT-PEMFCs before and after operation are compared on the microscale down to the nanoscale to understand operation related degradation. Cross-sectional samples from the fuel cell samples are investigated by SEM, while the changes of the individual particles are studied by STEM and TEM.

Two different HT-PEMFCs were studied: (i) HT-PEMFC non-operated (HT_non_operated). This FC has not suffered any operational-related degradation and will be used as reference (as-produced state). (ii) HT-PEMFC operated (HT_operated) which was operated for 12 000 h in a FC stack.

Moreover, three different regions from each cell were analysed in order to study the degradation rate across the cell. The samples were cut with a scalpel from each region of the FC:

(i) The first sample was taken close to the cathode inlet of the cell.

(ii) The second region is located in the middle of the FC (equidistant from both inlets).

(iii) The third sample was taken from the anode inlet region of the cell.

The scale bar of the SEM images cannot be displayed as well as the at% composition since some components of the investigated HT-PEMFC are protected by a patent. Nevertheless, all the images were taken with the same magnification, thus the relative thickness of the different layer can be compared. Furthermore, all SEM images are oriented with the cathode catalyst layer on top and the anode catalyst layer on bottom.

4.2. SEM characterization

SEM allows the characterization of the surface, structure, topography and microstructure of the FCs while EDX is used to analyze the elemental composition. Using secondary electrons (SE) the thickness and the topography of the layers from the FCs can be evaluated. Moreover, BSE imaging is based on the atomic number contrast (*Z*-contrast).[43] Since the catalyst particles in the anode and cathode are different they can be easily distinguished by BSE imaging. The SEM micrographs and EDX compositions maps were acquired in a Zeiss Sigma 500 operated at 15 kV.

4.3. STEM characterization

STEM allows the in-depth characterization of morphology, size and composition changes of the catalytic NPs. Titan Themis microscope (Thermo Fisher Scientific) operated at 300 kV, equipped with a probe corrector was used. STEM data was recorded on a metal–oxide–semiconductor (CMOS) camera (4k × 4k pixels). High angle annular dark field (HAADF) images (72–352 mrad) and EDX measurements were achieved with currents of 100 pA using a convergence semi-angle of 23.8 mrad (beam size ~ 0.1 nm). For each catalytic layer up to 100 NPs were analysed.

4.3. TEM characterization

TEM images and corresponding selected area electron diffraction pattern were taken to correlate the size and crystalline structure from the different catalytic NPs. A Titan Themis microscope (Thermo Fisher Scientific) operated at 300 kV, equipped with an image corrector was used. TEM data was recorded on a metal–oxide–semiconductor (CMOS) camera (4k × 4k pixels).

5. Conclusions

Microscale degradation mechanisms in HT-PEMFC by SEM, STEM and EDX were studied. HT-PEMFC operated during

12 000 h inside a fuel cell stack was investigated and compared with a non-operated HT-PEMFC. Two operation-related degradation mechanisms were found: thinning of the functional layers and catalyst material redistribution. A thinning of the CLs with a significantly higher level of degradation on the cathode side compared to the anode side was observed, due to the harsher operation conditions at the cathode side. The CLs deterioration can be a result of a degradation of the support material *via* carbon corrosion or/and to a degradation of the catalyst material due to the oxidation of Pt and Ru. Furthermore, a thinning process was detected for the membrane layer which is as well affected by the oxidation agents such as H_2O_2 or/and HO_2^-. Moreover, during HT-PEMFC operation, catalyst material was dissolved from the CLs and redistributed within the fuel cell.

Author contributions

Miquel Vega Paredes: SEM investigation, manuscript writing, data analysis & discussion. Alba Garzón Manjón: (S)TEM investigation and data analysis, manuscript writing, conception of the work, discussion, supervision. Bjoern Hill: SEM investigation, data analysis & discussion, editing of the manuscript. Torsten Schwarz: SEM investigation, editing of the manuscript. Nicolas A. Rivas: discussion and editing of the manuscript. Tilman Jurzinsky: fuel cell manufacturing, discussion, editing of the manuscript. Katharina Hengge: fuel cell manufacturing, discussion, editing of the manuscript. Florian Mack: fuel cell manufacturing, discussion, editing of the manuscript. Christina Scheu: conception of the work, discussion, supervision, editing of the manuscript. All authors approved the final version of the manuscript.

Conflicts of interest

There authors declare no conflict of interest.

Acknowledgements

The research project (FKZ 03ETB018C) was supported by the Federal Ministry for Economic Affairs and Climate Action based on a decision taken by the German Bundestag. Dr Benedikt Distl is acknowledged for his help during the writing process. Open Access funding provided by the Max Planck Society.

Notes and references

1 IEA, Data and Statistics, https://www.iea.org/data-and-statistics/data-browser?country=WORLD&fuel=CO2emissions&indicator=CO2BySector.
2 O. Z. Sharaf and M. F. Orhan, *Renewable Sustainable Energy Rev.*, 2014, **32**, 810–853.
3 O. Bethoux, *Energies*, 2020, **13**(21), 5843.
4 N. Sazali, W. N. Wan Salleh, A. S. Jamaludin and M. N. Mhd Razali, *Membranes*, 2020, **10**(5), 99.
5 T. Sutharssan, D. Montalvao, Y. Kang, W. Wang, C. Pisac and H. Elemara, *Renewable Sustainable Energy Rev.*, 2017, **75**, 440–450.
6 R. Zhu, L. Xing and Z. Tu, *Energy Convers. Manage.*, 2022, **253**, 115182.
7 D. Y. Chung, H. Kim, Y. Chung, M. J. Lee, S. J. Yoo, A. D. Bokare, W. Choi and Y. Sung, *Sci. Rep.*, 2014, 1–5.
8 H. Yamada, H. Kato and K. Kodama, *J. Electrochem. Soc.*, 2020, **167**, 084508.
9 C. Jackson, O. Conrad and P. Levecque, *Electrocatalysis*, 2017, **8**, 224–234.
10 N. Ramaswamy, S. Kumaraguru, R. S. Kukreja, D. Groom, K. Jarvis and P. Ferreira, *J. Electrochem. Soc.*, 2021, **168**, 124512.
11 K. Hengge, C. Heinzl, M. Perchthaler, D. Varley, T. Lochner and C. Scheu, *J. Power Sources*, 2017, **364**, 437–448.
12 K. Yu, D. J. Groom, X. Wang, Z. Yang, M. Gummalla, S. C. Ball, D. Myers and P. J. Ferreira, *Microsc. Microanal.*, 2014, **20**, 482–483.
13 S. Rasouli, R. A. Ortiz Godoy, Z. Yang, M. Gummalla, S. C. Ball, D. Myers and P. J. Ferreira, *J. Power Sources*, 2017, **343**, 571–579.
14 V. Bandlamudi, P. Bujlo, C. Sita and S. Pasupathi, *Mater. Today: Proc.*, 2018, **5**, 10602–10610.
15 S. Rasouli, M. R. Berber, I. H. Hafez, T. Fujigaya, P. Ferreira and N. Nakashima, *Microsc. Microanal.*, 2015, **21**, E2–E3.
16 K. Hengge, T. Gänsler, E. Pizzutilo, C. Heinzl, M. Beetz, K. J. J. Mayrhofer and C. Scheu, *Int. J. Hydrogen Energy*, 2017, **42**, 25359–25371.
17 K. A. Hengge, C. Heinzl, M. Perchthaler, S. Geiger, K. J. J. Mayrhofer and C. Scheu, *Cryst. Growth Des.*, 2017, **17**, 1661–1668.
18 B. T. Sneed, D. A. Cullen, K. S. Reeves, O. E. Dyck, D. A. Langlois, R. Mukundan, R. L. Borup and K. L. More, *ACS Appl. Mater. Interfaces*, 2017, **9**, 29839–29848.
19 F. Du, T. A. Dao, A. Bauer, M. Obermaier, T. J. Schmidt and A. Orfanidi, *Electrochim. Acta*, 2022, **402**, 139537.
20 Y. Ishigami, K. Takada, H. Yano, J. Inukai, M. Uchida, Y. Nagumo, T. Hyakutake, H. Nishide and M. Watanabe, *J. Power Sources*, 2011, **196**, 3003–3008.
21 T. E. O'Brien, S. Herrera, D. A. Langlois, N. N. Kariuki, H. Yu, M. J. Zachman, D. J. Myers, D. A. Cullen, R. L. Borup and R. Mukundan, *J. Electrochem. Soc.*, 2021, **168**, 054517.
22 E. Padgett, V. Yarlagadda, M. E. Holtz, M. Ko, B. D. A. Levin, R. S. Kukreja, J. M. Ziegelbauer, R. N. Andrews, J. Ilavsky, A. Kongkanand and D. A. Muller, *J. Electrochem. Soc.*, 2019, **166**, F198–F207.
23 S. Martin, P. L. Garcia-Ybarra and J. L. Castillo, *Appl. Energy*, 2017, **205**, 1012–1020.
24 R. Lin, X. Cui, J. Shan, L. Técher, F. Xiong and Q. Zhang, *Int. J. Hydrogen Energy*, 2015, **40**, 14952–14962.
25 M. Obermaier, M. Rauber, A. Bauer, T. Lochner, F. Du and C. Scheu, *Fuel Cells*, 2020, **20**, 394–402.

26 S. Ramakrishnan, K. Ramya and N. Rajalakshmi, in *PEM Fuel Cells*, ed. G. Kaur, Elsevier, 2022, pp. 223–242.
27 T. Lochner, R. M. Kluge, J. Fichtner, H. A. El-sayed, B. Garlyyev and A. S. Bandarenka, *ChemElectroChem*, 2020, 3545–3568.
28 J. Durst, A. Lamibrac, F. Charlot, J. Dillet, L. F. Castanheira, G. Maranzana, L. Dubau, F. Maillard, M. Chatenet and O. Lottin, *Appl. Catal., B*, 2013, **138–139**, 416–426.
29 J. Li, L. Yang, Z. Wang, H. Sun and G. Sun, *Int. J. Hydrogen Energy*, 2021, **46**, 24353–24365.
30 A. Laconti, H. Liu, C. Mittelsteadt and R. McDonald, *ECS Trans.*, 2006, **1**, 199–219.
31 M. Chandesris, L. Guetaz, P. Schott, M. Scohy and S. Escribano, *J. Electrochem. Soc.*, 2018, **165**(6), F3290–F3306.
32 R. Borup, J. Meyers, B. Pivovar, Y. S. Kim, R. Mukundan, N. Garland, D. Myers, M. Wilson, F. Garzon, D. Wood, P. Zelenay, K. More, K. Stroh, T. Zawodzinski, J. Boncella, J. E. McGrath, M. Inaba, K. Miyatake, M. Hori, K. Ota, Z. Ogumi, S. Miyata, A. Nishikata, Z. Siroma, Y. Uchimoto, K. Yasuda, K. I. Kimijima and N. Iwashita, *Chem. Rev.*, 2007, **107**, 3904–3951.
33 Y. Oono, A. Sounai and M. Hori, *J. Power Sources*, 2012, **210**, 366–373.
34 C. J. Mcdonnell-worth and D. R. MacFarlane, *Aust. J. Chem.*, 2018, **71**(10), 781–788.
35 A. Sorrentino, K. Sundmacher and T. Vidakovic-koch, *Energies*, 2020, **13**(21), 5825.
36 T. Ossiander, M. Perchthaler, C. Heinzl and C. Scheu, *J. Power Sources*, 2014, **267**, 323–328.
37 N. Macauley, D. D. Papadias, J. Fairweather, D. Spernjak, D. Langlois, R. Ahluwalia, K. L. More, R. Mukundan and R. L. Borup, *J. Electrochem. Soc.*, 2018, **165**, F3148–F3160.
38 M. F. Labata, G. Li, J. Ocon and P.-Y. A. Chuang, *J. Power Sources*, 2021, **487**, 229356.
39 K. Yasuda, A. Taniguchi, T. Akita, T. Ioroi and Z. Siroma, *Phys. Chem. Chem. Phys.*, 2006, **8**, 746–752.
40 Y. Sun, S. Polani, F. Luo, S. Ott, P. Strasser and F. Dionigi, *Nat. Commun.*, 2021, **12**, 1–14.
41 P. J. Ferreira, G. J. la O', Y. Shao-Horn, D. Morgan, R. Makharia, S. Kocha and H. A. Gasteiger, *J. Electrochem. Soc.*, 2005, **152**, A2256.
42 J. Zhang, B. A. Litteer, W. Gu, H. Liu and H. A. Gasteiger, *J. Electrochem. Soc.*, 2007, **154**, B1006.
43 A. Garzón-Manjón, L. Christiansen, I. Kirchlechner, B. Breitbach, C. H. Liebscher, H. Springer and G. Dehm, *J. Alloys Compd.*, 2019, **794**, 203–209.